

# EAGLE: Expert-Augmented Attention Guidance for Tuning-Free Industrial Anomaly Detection in Multimodal Large Language Models

Xiaomeng Peng Xilang Huang Seon Han Choi

Ewha Womans University

{xiaomeng, seonhan.choi}@ewha.ac.kr, {huangxilang901}@gcc.edu.cn

## Abstract

Industrial anomaly detection is important for smart manufacturing, but many deep learning approaches produce only binary decisions and provide limited semantic explanations. Multimodal large language models (MLLMs) can potentially generate fine-grained, language-based analyses, yet existing methods often require costly fine-tuning and do not consistently improve anomaly detection accuracy compared to lightweight specialist detectors. We propose expert-augmented attention guidance for industrial anomaly detection in MLLMs (EAGLE), a tuning-free framework that integrates outputs from expert model to guide MLLMs toward both accurate detection and interpretable anomaly descriptions. We further study how EAGLE affects MLLMs internals by examining the attention distribution of MLLMs to the anomalous image regions in the intermediate layers. We observe that successful anomaly detection is associated with increased attention concentration on anomalous regions, and EAGLE tends to encourage this alignment. Experiments on MVTEC-AD and VisA show that EAGLE improves anomaly detection performance across multiple MLLMs without any parameter updates, achieving results comparable to fine-tuning based methods. Code is available at <https://github.com/shengtun/Eagle>

## 1. Introduction

In intelligent manufacturing scenarios, Industrial Anomaly Detection (IAD) is a core task for ensuring product quality and operational safety. Although deep learning based IAD models have achieved high performance on multiple benchmark datasets, they still suffer from a fundamental limitation in real-world deployment: their outputs are typically restricted to binary decisions, lacking interpretable semantic information such as anomaly type identification, precise localization, and descriptive explanations [18]. This limitation makes it difficult to effectively support on-site troubleshooting and quality control.

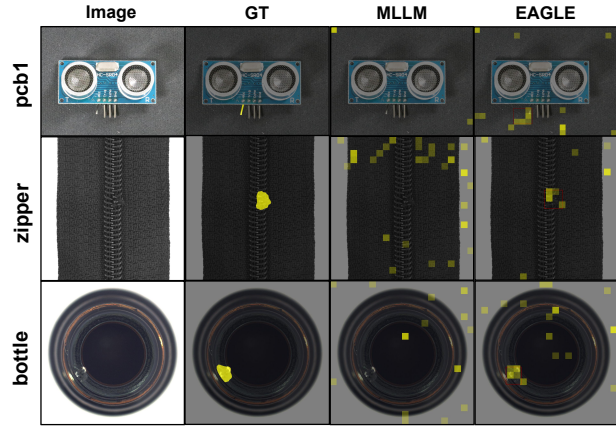


Figure 1. Attention map visualizations from Qwen2.5-VL-7B on the MVTEC-AD and VisA dataset. Compared with the original model, our framework guides the model to consistently focus on anomalous regions.

To bridge this semantic gap, recent studies have explored introducing Multimodal Large Language Models (MLLMs) into the IAD domain. Early exploratory works (e.g., AnomalyGPT [12], Myriad [24]) tend to design task-specific MLLMs architectures tailored for anomaly detection. However, when confronted with the sparsity of defect data in industrial settings, such approaches are prone to overfitting and incur substantial pre-training and instruction-tuning costs, ultimately resulting in a low return on investment [18]. With the rapid improvement of general-purpose MLLMs in terms of reasoning capability and generalization, subsequent research has shifted toward leveraging pretrained MLLMs and adapting them to IAD tasks via supervised fine-tuning (SFT) [26, 35] or Group Relative Policy Optimization (GRPO) [13, 25, 41, 42]. While these methods provide enhanced interpretability such as anomaly explanation and reasoning, they still require high instruction-tuning costs. Critically, they underperform specialized deep learning methods on anomaly detection accuracy, which remains the most essential metric in industrial practice. This limitation substantially constrains the practical applicability of

MLLMs in IAD.

To overcome these limitations, we propose EAGLE, a tuning-free framework that synergizes expert models with MLLMs to achieve high detection accuracy while enabling semantic anomaly analysis.

**A critical challenge in integrating expert models with MLLMs is determining when and how to provide visual prompts.** Prior frameworks [12, 18, 24] typically inject visual cues (e.g., anomaly maps) from expert models indiscriminately across all samples. However, since expert models also generate anomaly maps for normal images—where certain local regions may exhibit high responses and be highlighted with bounding boxes—this can lead to over-representation of visual signals, biasing MLLMs toward false positive predictions. To mitigate this issue, **our framework selectively provides visual prompts only for images identified as anomalous by the expert model.** This strategy, however, typically relies on manually selected decision thresholds in expert models for distinguishing normal from abnormal samples.

To address these requirements, we introduce the **Distribution-Based Thresholding (DBT)** mechanism, which leverages discarded patch information from the expert model’s memory bank construction (e.g., PatchCore [31]) to estimate the anomaly score distribution of normal samples. Based on this distribution, DBT automatically derives statistically reliable decision thresholds. During inference, this threshold determines whether expert-generated visual prompts are selectively provided to the MLLMs. At the same time, to further strengthen the guidance signal, we additionally incorporate corresponding binary textual priors (e.g., “*predicted as normal*” or “*predicted as abnormal*”), which, together with the selected visual prompts, are injected into the MLLMs to guide reasoning.

While such textual priors provide a concise and interpretable way to convey expert judgments, their effectiveness is inherently constrained by the strong language bias of MLLMs. A fundamental issue with MLLMs is their inherent tendency to prioritize linguistic information over visual information [1, 7, 34]. By analyzing hidden states and the attention distribution over the image from intermediate transformer layers during answer generation, we observe that even when MLLMs concentrate attention to ground-truth anomalous regions in intermediate layers, erroneous textual priors from the expert model can override this visual evidence in later layers, leading to incorrect predictions. Accordingly, we introduce the Confidence-Aware Attention Sharpening (CAAS) mechanism that selectively amplifies visual attention when expert predictions are uncertain. This enables MLLMs to rely more on visual information when textual priors are unreliable, mitigating hallucinations caused by erroneous textual priors guidance.

Our experimental analysis further shows that samples

with correct predictions tend to exhibit higher attention concentration on ground-truth defect regions, indicating a strong correlation between attention alignment and prediction accuracy. As illustrated in Fig. 1, EAGLE is able to redirect the attention of MLLMs toward anomalous regions, suggesting improved focus on relevant visual evidence during answer generation.

Experimental results on mainstream industrial anomaly detection datasets MVTec-AD[4] and VisA[45] show that EAGLE consistently improves the anomaly detection performance of multiple MLLMs and achieves competitive and often superior results compared to fine-tuning based methods on key metrics such as accuracy and F1 score.

## 2. Related work

### 2.1. Industrial Anomaly Detection

Existing approaches fall into two main categories. **Reconstruction-based methods** [17, 38] train generative models to reconstruct normal images, flagging samples with high reconstruction errors as anomalies. **Feature embedding methods** leverage pretrained visual encoders to extract image features, employing memory banks [22, 31] or student-teacher architectures [3, 5] to model the feature space of normality. Anomalies are identified by measuring feature space deviations between test samples and normal prototypes.

Recently, vision-language models (VLMs) have shown promise for IAD. Methods such as WinCLIP [16], AnomalyCLIP [43], and PromptAD [23] exploit pretrained models like CLIP for few-shot and zero-shot anomaly detection. However, these methods provide limited semantic explanations and interpretability for detected anomalies.

### 2.2. Multimodal Large Language model for IAD

Most existing studies focus on applying pre-trained MLLMs to general vision–language tasks, such as visual question answering [11, 15, 32], and image captioning [27, 37], where MLLMs have demonstrated impressive performance.

However, applying MLLMs to industrial anomaly detection (IAD) remains challenging. Some studies [12, 19, 24, 35, 41] have begun to explore fine-tuning MLLMs using anomaly detection datasets to enhance their capabilities in emotion understanding and reasoning. AnomalyGPT [12] designs a language-guided image decoder to generate anomaly maps and employs a prompt learner to automatically acquire expert prompts for the LLM. Myriad [24] proposes to regard existing IAD models as vision experts (VEs) for anomaly detection tasks and establishes a novel large multimodal model that integrates these vision experts for industrial scenarios. More recently, some approaches [6, 39, 42] adopt GRPO to align MLLMs with IAD tasks via interactive feedback. In addition, several works [8, 20, 30, 40] explore the direct application of MLLMs to IAD tasks without any fine-tuning.

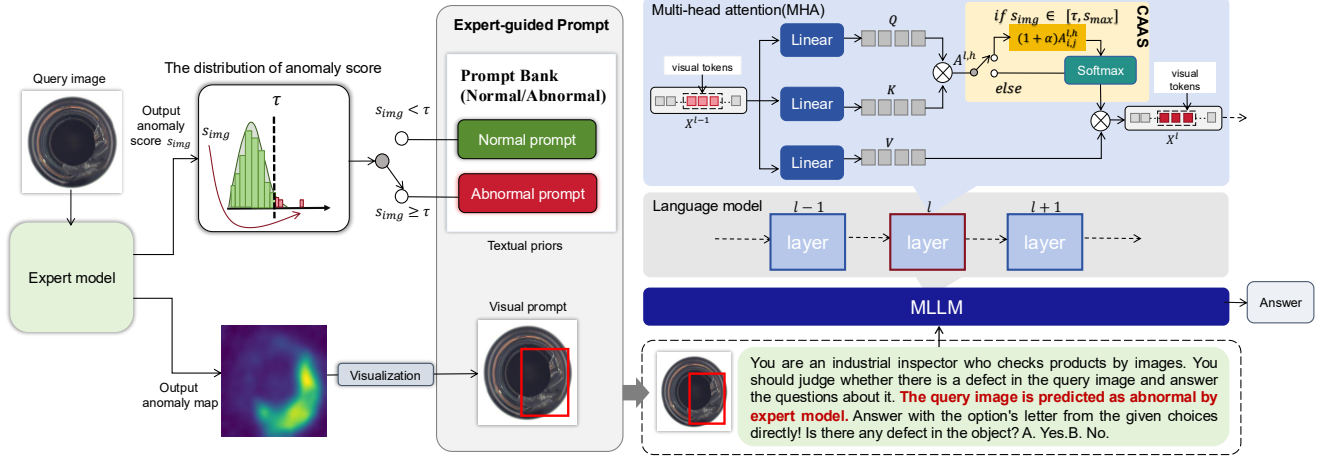


Figure 2. **Pipeline of EAGLE.** Given a query image, the expert model outputs an image-level anomaly score and a pixel-level anomaly map. The anomaly score is compared with a threshold  $\tau$  estimated by the proposed DBT mechanism (see §3.2), which determines whether the image is predicted as normal or abnormal and controls the selective injection of expert-generated visual prompts as well as the selection of corresponding textual prompts. When the anomaly score falls into the low-confidence region  $[\tau, s_{\max}]$ , the CAAS mechanism (see §3.3) conditionally enhances attention to visual tokens. The combined textual priors and visual prompts guide the MLLMs to produce the final anomaly prediction. The attention logits are defined as  $A^{l,h} = QK^T / \sqrt{d_k}$ , and  $X^{l-1}$  and  $X^l$  represent the input and output of the MHA at layer  $l$ , respectively.

Despite recent progress, these approaches generally require extensive training resources while still exhibiting limited performance on the core anomaly classification task. In contrast, this paper proposes a tuning-free framework that improves the anomaly detection capability of MLLMs without any additional parameter updates.

### 3. Method

#### 3.1. Framework Overview

We propose EAGLE, a tuning-free framework for anomaly detection. The framework comprises two core components: (1) a PatchCore-based expert model that performs preliminary anomaly detection and transforms the detection results into visual and textual prompt, and (2) a Multimodal Large Language Model (MLLM) that receives the visual and textual prompts generated by the expert model for reasoning. Figure 2 illustrates the complete framework pipeline.

To avoid fine-tuning overhead, we introduce two key mechanisms. The Distribution-Based Thresholding (DBT) mechanism (§3.2) transforms expert model outputs into prompts suitable for MLLMs input by estimating a decision threshold from anomaly score distributions on normal samples. This threshold classifies test samples and determines the corresponding visual prompts and textual prompts (linguistic priors) for MLLMs input. The CAAS mechanism (§3.3) identifies low-confidence predictions from the expert model and selectively amplifies visual token attention in MLLMs intermediate layers. By strengthening visual evidence, CAAS prevents the MLLMs from over-relying on erroneous linguistic priors, enabling more accurate correc-

tion of expert model misclassifications.

#### 3.2. Expert Model with Distribution-Based Thresholding

##### 3.2.1. Preliminaries of Expert model

The expert model adopts the PatchCore [31] architecture. Following its standard procedure, a pre-trained feature extractor (e.g., WideResNet50) is used to extract feature maps  $\mathcal{F}_i = \phi_i \in \mathbb{R}^{C \times H \times W}$  from each training image  $x_i$ . Patch features from all training samples are aggregated into a patch feature set  $\mathcal{F}$ , from which a memory bank  $\mathcal{M}$  is constructed via a coresets sampling algorithm  $\mathcal{G}$ .

$$\mathcal{M} = \mathcal{G}(\mathcal{F}), \quad \mathcal{M} \subset \mathcal{F} \quad (1)$$

In the inference stage, given a test image  $x_t$ , patch-level features  $\mathcal{F}_t$  are extracted using the same feature extractor as in training. For each patch feature  $f_t^{(h,w)} \in \mathcal{F}_t$ , its anomaly score  $s_t^{(h,w)}$  is defined as the Euclidean distance to its nearest neighbor in the memory bank  $\mathcal{M}$ :

$$m^* = \arg \min_{m \in \mathcal{M}} \|f_t^{(h,w)} - m\|_2, \quad (2)$$

$$s_t^{(h,w)} = \|f_t^{(h,w)} - m^*\|_2. \quad (3)$$

Here,  $(f_t^{(h,w)}, m^*)$  denotes a test patch and its corresponding nearest neighbor in  $\mathcal{M}$ . The image-level anomaly score  $s_{img}$  is defined as the maximum patch-level score over all spatial locations:

$$s_{img}^t = \max(s_t^{(1,1)}, s_t^{(1,2)}, \dots, s_t^{(h,w)}). \quad (4)$$

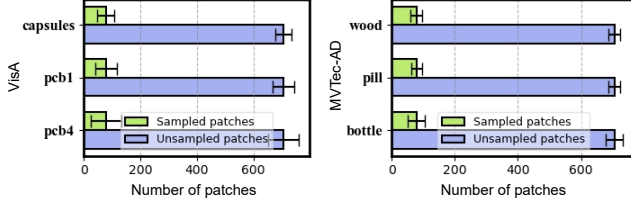


Figure 3. Average number of sampled and unsampled patches per training image for different classes during memory bank construction.

### 3.2.2. Distribution-Based Thresholding Mechanism

In PatchCore, anomaly scores are computed as distances between test patch features and the memory bank, while the threshold is typically selected manually. To automatically compute thresholds before testing, we propose the DBT mechanism, which estimates image-level decision thresholds by modeling the distribution of anomaly scores using unsampled patch features during memory bank construction. Fig. 5 provides an overview of the DBT pipeline.

A key observation motivating DBT is that only a small fraction of patch features are retained in the memory bank, while the majority are discarded during coreset sampling. These discarded features, although not stored in the memory bank, are still extracted from normal training images and thus encode rich information about the normal data distribution.

Formally, for each training image  $x_i \in X^{\text{train}} = \{x_1, x_2, \dots, x_N\}$ , where all samples are normal, we denote the set of sampled patch features as  $P_i^{(s)}$  and the set of unsampled patch features as

$$P_i^{(un)} = \mathcal{F}_i \setminus P_i^{(s)}, \quad (5)$$

where  $\mathcal{F}_i = \{\phi_i^{(h,w)}\}$  represents the complete set of patch features extracted from  $x_i$ .

As illustrated in Fig. 3, we analyze the proportion of sampled and unsampled patches per training image during memory bank construction on representative classes. The results show that, on average, only about 10% of patches are selected into the memory bank, while the unsampled patches account for approximately 90% of all extracted features.

Following the anomaly score formulation (Eqs. 2, 3, and 4), the anomaly score of a patch is defined as its nearest-neighbor distance to the memory bank  $\mathcal{M}$ , and the image-level anomaly score is computed as the maximum over all patch-level scores. Under this formulation, we make the following observation.

**For a normal training sample, the image-level anomaly score can be determined solely by the unsampled patches  $P_i^{(un)}$ .** Intuitively, the patch  $f_i^*$  that attains the maximum anomaly score for an image is unlikely to be included in the memory bank. If  $f_i^*$  were sampled into  $\mathcal{M}$ , its anomaly score would reduce to the distance between itself and an identical

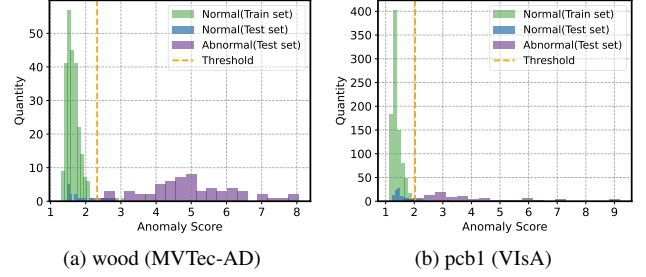


Figure 4. Anomaly score distributions across datasets. Normal training (green), normal test (blue), and abnormal test (purple) samples are shown. Additional results are included in the Appendix 6.3.1.

entry, i.e.,  $\|f_i^* - m^*\|_2 = 0$  with  $m^* = f_i^*$ . Therefore, for normal training samples, the image-level anomaly score typically arises from patches that are not selected into the memory bank.

As a result, we can compute the image-level anomaly scores for all normal training samples and denote them as  $\mathcal{S} = \{s_{img}^1, s_{img}^2, \dots, s_{img}^N\}$ . As shown in Fig. 4, the green histogram corresponds to the anomaly scores of normal training images, while the blue histogram represents those of normal test images. We observe that the distribution estimated from the training set covers most normal test samples, owing to the large number of normal training images. In contrast, images containing defects produce substantially higher anomaly scores, as defect regions yield large patch-level distances that exceed the normal score distribution, as

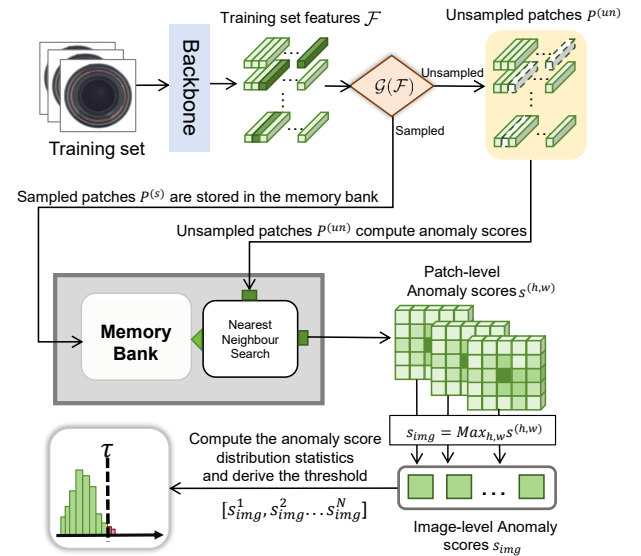


Figure 5. Illustration of the DBT mechanism. Normal training images are converted into patch-level features  $\mathcal{F}$ , which are stored in a memory bank constructed via greedy coreset sampling  $\mathcal{G}$ . For each training image  $x_i$ , its unsampled patch set  $P_i^{(un)}$  is used to compute the image-level anomaly score through nearest-neighbor search (Eqs. 2, 3).

illustrated by the purple histogram in Fig. 4.

The threshold  $\tau$  is determined adaptively based on the mean  $\mu_s$  and standard deviation  $\sigma_s$  of the anomaly score distribution in the training set:  $\tau = \mu_s + \kappa \cdot \sigma_s$  where  $\kappa$  is a parameter that controls the strictness of the decision boundary, and is set to  $\kappa = 3$  in our experiments. Regions with anomaly scores higher than  $\tau$  are grouped as anomalous, while those below  $\tau$  are grouped as normal.

### 3.2.3. Conditional Prompt Selection for MLLMs

During inference, the expert model provides two types of guidance to the MLLMs in the form of visual and textual prompts.

**Visual prompt:** We upsample the patch-level anomaly scores obtained from Eqs. 2, 3 to the original image resolution to construct an anomaly map. Based on this map, potential defect regions are localized and highlighted by drawing red bounding boxes on the input image (See details in the Appendix. 6.3.1). Since the expert model may also highlight regions in normal images, these visual cues can mislead the MLLMs. Therefore, visual prompts are provided only for images predicted as anomalous.

**Textual prompt:** For each test image, we compare its image-level anomaly score  $s_{img}^t$  (Eq. 4) with the threshold  $\tau$  to select the corresponding textual prior. When  $s_{img}^t < \tau$ , the prior reads “*This image is predicted as normal.*”; when  $s_{img}^t \geq \tau$ , it reads “*This image is predicted as abnormal.*”

## 3.3. MLLMs with Confidence-Aware Attention Scaling

### 3.3.1. Preliminaries of MLLMs

In MLLMs, visual tokens extracted by a vision encoder and a projector are concatenated with text tokens, forming a unified input sequence  $\mathbf{X} = [\mathbf{X}_v; \mathbf{X}_t]$ , which is then fed into the language model. The language model is composed of multiple Transformer layers, among which a core component is the multi-head attention (MHA) mechanism.

$$x_i^l = x_i^{l-1} + \sum_{h=1}^H \text{MHA}^{l,h}(x_i^{l-1}), \quad (6)$$

$$\text{MHA}^{l,h}(x_i^{l-1}) = \sum_{j \leq i} A_{i,j}^{l,h} x_j^{l-1} W_V^{l,h}, \quad (7)$$

where  $x_i^{l-1}$  and  $x_i^l$  represent the input and output of the  $i$ -th token of the MHA at layer  $l$ , respectively, and  $H$  is the number of attention heads. Eq.7 represents the individual input  $x_i^{l-1}$  and its previous tokens attention contributions  $X_{\leq i}^{l-1} = \{x_1^{l-1}, \dots, x_i^{l-1}\}$ . Here,  $A_{i,j}^{l,h}$  denotes the attention weight from  $x_j^{l-1}$  to  $x_i^{l-1}$ , which can be interpreted as the degree to which  $x_i^{l-1}$  attends to  $x_j^{l-1}$ .  $W_V$  represents the value matrix.

Finally, for a sequence of length  $L$ , the probability of generating the answer  $\mathbf{X}_a$  is computed in an autoregressive manner:

$$p(\mathbf{X}_a | \mathbf{X}_v, \mathbf{X}_t) = \prod_{i=1}^L p(x_i | \mathbf{X}_v, \mathbf{X}_{t,<i}, \mathbf{X}_{a,<i}), \quad (8)$$

where  $\mathbf{X}_{t,<i}$  and  $\mathbf{X}_{a,<i}$  denote the text tokens and previously generated answer tokens before position  $i$ , respectively.

From this formulation, it follows that attention weights play a critical role in controlling how visual and textual information is aggregated, and modifying these weights can influence the model’s final prediction.

### 3.3.2. Language Prior Dominance Problem

Prior work[7, 21, 33, 36] has shown that MLLMs allocate significantly more attention to textual tokens than visual tokens, which we also observe in our experiments. As shown in Fig. 7(b), when the expert model provides incorrect textual priors (e.g., misclassifying a defective sample as “*predicted as normal*”), the MLLMs tends to over-trust this linguistic information.

To analyze how incorrect textual priors influence MLLMs decision-making, we conduct a controlled experiment using a defective image from the *wood* class in MVTEC-AD. As shown in Fig. 7 and Fig. 6, we examine both the layer-wise prediction dynamics and the corresponding visual attention patterns under three settings: (a) the original MLLMs without expert guidance, (b) EAGLE without CAAS, and (c) EAGLE with CAAS (introduced in §3.3.3). In settings (b) and (c), the expert model intentionally provides an incorrect textual prior by misclassifying a defective sample as “*predicted as normal*,” allowing us to probe how MLLMs respond to conflicting linguistic and visual cues.

Across all three settings, a consistent pattern emerges in the intermediate layers ( $9 \leq l \leq 15$ ), where the probability of the correct answer exceeds that of the incorrect one. This behavior is observed even under settings Fig. 7(b) and (c), where an incorrect textual prior is provided, suggesting that the MLLMs may have begun to rely on visual evidence that supports the correct decision. However, in setting 7(b), this visually grounded preference is gradually overridden in later layers by the misleading textual prior, ultimately leading to an incorrect prediction.

### 3.3.3. Confidence-Aware Attention Scaling Mechanism

Follow prior work [7, 36], we introduce CAAS, which enhances MLLMs attention weights to visual tokens when the expert model is uncertain, thus reducing the influence of incorrect textual priors.

We define the low-confidence region as cases where the anomaly score  $s_{img}$  of the test sample falls within the interval  $[\tau, s_{max}]$ , where  $\tau$  is the threshold estimated by DBT and  $s_{max}$  is the maximum anomaly score among normal samples

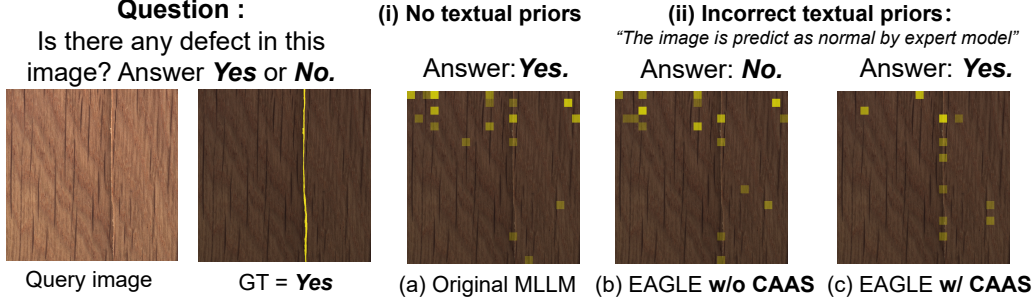


Figure 6. Attention map visualizations corresponding to the layer-wise prediction dynamics in Fig. 7 under different settings.

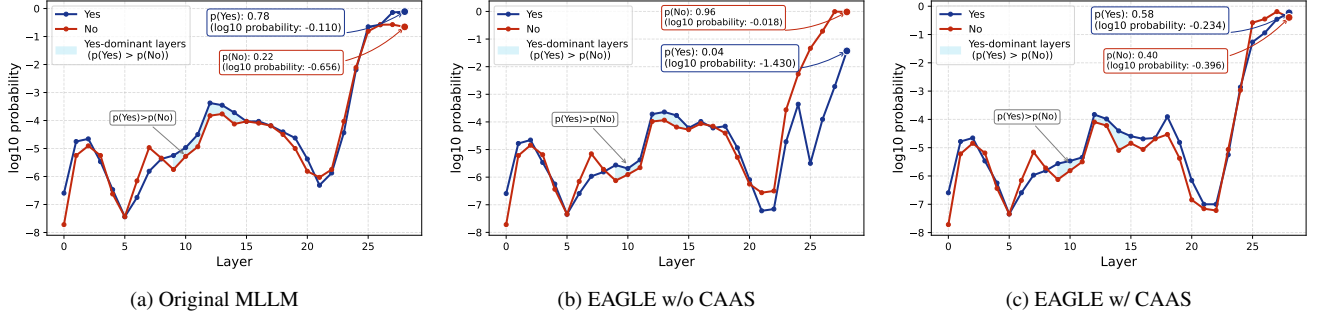


Figure 7. Layer-wise log probability evolution of candidate answers (“Yes” and “No”) under incorrect textual priors for anomaly detection. Results are obtained on the *wood* class of the MVTec-AD dataset and correspond to the attention visualizations shown in Fig 6.

in the training set. This interval corresponds to the overlap between normal and abnormal distributions, where the judgment of the expert model has high uncertainty. When a test sample is detected to be in the low-confidence region, CAAS is activated.

Indiscriminately amplifying visual attention does not necessarily correct the MLLMs focus and may instead amplify spurious signals or introduce additional noise[7]. Based on our earlier observation (in §3.3.2) that intermediate layers ( $9 \leq l \leq 15$ ) are highly sensitive to visual reasoning, we selectively adjust attention allocation only in these layers. Specifically, for the attention weight  $A_{i,j}^{(l,h)}$  at position  $(i, j)$  in layer  $l$  (where  $l$  denotes layer index and  $h$  denotes attention head index), the adjusted attention matrix is computed as:

$$A_{i,j}^{(l,h)} = \begin{cases} (1 + \alpha) \cdot A_{i,j}^{(l,h)} & \text{if } j \in \mathcal{I} \\ A_{i,j}^{(l,h)} & \text{otherwise} \end{cases}, \text{ if } s_{img} \in [\tau, s_{max}], \quad (9)$$

where  $\mathcal{I}$  represents the index set of all visual tokens.  $\alpha$  is the scaling factor (set to 0.6 in this work).

Fig. 7(c) illustrates the effect of applying CAAS. Compared to case Fig. 7(b) without CAAS, the prediction dynamics in later layers exhibit a clear reversal, where the probability of the correct answer increases steadily while the incorrect one gradually declines around the 27-th layer, leading to a correct final prediction. This change is consistent

with the attention patterns shown in Fig. 6, where CAAS promotes more concentrated attention on defect regions.

## 4. Experiments

### 4.1. Experiment Details

**MLLMs backbone.** We evaluate EAGLE on five diverse MLLMs to demonstrate its generalizability, including LLaVA-1.5-7B[28], LLaVA-NeXT-7B[29], Qwen2.5-VL-7B[2], InternVL3-8B[44], MiniCPM-8B[14].

**Implementation Detail.** We adopt PatchCore[31] with WideResNet-50 as the backbone. Images are processed at a resolution of  $256 \times 256$  and center-cropped to  $224 \times 224$  for PatchCore, while visual prompts are restored to the original image resolution before being fed into the MLLMs. For the experiments reported in Tab. 1 and 2, we set the parameter  $\alpha = 0.6$ . For original MLLMs, we follow the 1-shot+ setting proposed in [18], where the most similar normal image is retrieved from the training set and used as a template to provide additional visual context during inference. All experiments were conducted on a single RTX 3090 24GB GPU.

**Datasets.** We evaluate our framework on MVTec-AD[4] and VisA[45], two widely used industrial anomaly detection benchmarks following the one-class learning setting, which encompass diverse industrial objects and textures and reflect realistic inspection scenarios.

Table 1. Quantitative comparison between MLLMs and MLLMs with EAGLE on the MVTec-AD and VisA datasets. Baseline MLLMs follow a 1-shot<sup>+</sup> template image setting(see §4.1).

Method	Scale	MVTec-AD				VisA			
		Accuracy	Precision	Recall	F1	Accuracy	Precision	Recall	F1
LLaVA-1.5	7B	61.6	79.2	72.3	71.9	58.4	75.0	26.5	32.8
<b>LLaVA-1.5 w/ours</b>	7B	<b>92.9</b>	<b>97.1</b>	<b>95.7</b>	<b>96.1</b>	<b>88.6</b>	<b>95.7</b>	<b>81.1</b>	<b>86.1</b>
LLaVA-NeXT	7B	69.8	99.5	40.2	50.9	59.0	80.8	18.8	27.9
<b>LLaVA-NeXT w/ours</b>	7B	<b>92.1</b>	<b>96.6</b>	<b>95.7</b>	<b>96.1</b>	<b>88.1</b>	<b>95.2</b>	<b>80.5</b>	<b>88.6</b>
MiniCPM-V4.5	8B	62.7	79.8	38.0	45.6	62.7	79.8	38.0	45.6
<b>MiniCPM-V4.5 w/ours</b>	8B	<b>93.4</b>	<b>97.3</b>	<b>95.8</b>	<b>96.3</b>	<b>88.2</b>	<b>95.8</b>	<b>80.5</b>	<b>85.6</b>
InternVL3	8B	83.9	91.2	89.7	90.0	74.2	89.6	58.6	66.1
<b>InternVL3 w/ours</b>	8B	<b>93.4</b>	<b>97.3</b>	<b>95.0</b>	<b>95.9</b>	<b>88.5</b>	<b>95.5</b>	<b>81.2</b>	<b>86.0</b>
Qwen2.5-VL	7B	85.9	95.0	83.9	88.3	76.0	89.2	61.2	69.4
<b>Qwen2.5-VL w/ours</b>	7B	<b>94.6</b>	<b>98.5</b>	<b>95.3</b>	<b>96.7</b>	<b>86.7</b>	<b>95.1</b>	<b>77.3</b>	<b>83.6</b>

Table 2. Comparison of our method with existing fine-tuning based and tuning-free approaches. Performance is evaluated using Accuracy (%). EAGLE is evaluated with InternVL3 as the MLLM backbone.

Method	MVTec-AD	VisA
<i>Fine-tuning based methods</i>		
AnomalyGPT	86.1 ± 1.1	77.4 ± 1.0
Myriad	87.4 ± 0.9	80.0 ± 0.4
<i>GRPO &amp; Fine-tuning based methods</i>		
LR-IAD	84.4 ± 0.0	87.6 ± 0.0
OmniAD	<b>96.0 ± 0.0</b>	86.6 ± 0.0
<i>Tuning-free methods</i>		
Echo	89.7 ± 0.0	76.8 ± 0.0
<b>EAGLE (Ours)</b>	<b>93.4 ± 0.0</b>	<b>88.5 ± 0.0</b>

**Experiment Metric.** We adopt a binary classification evaluation protocol: we pose the question “*Is there any defect in this image?*” to the MLLMs and determine the prediction by checking whether the generated text contains “*yes*” or its variants (e.g., “*abnormal*”, “*defect*”). Model performance is assessed using metrics: Accuracy, Precision, Recall, F1-score.

**Baseline.** We compare our approach with existing fine tuning based, GRPO-based, and training-free methods[8]. The fine tuning based methods includes specialized MLLMs for anomaly detection [12, 24], as well as MLLMs trained via GRPO or fine tuned on anomaly detection datasets[39, 42].

## 4.2. Quantitative Results

**Main Results on MVTec-AD and VisA.** Tab. 1 reports the performance of EAGLE across different MLLM backbones on the MVTec-AD and VisA. EAGLE leads to reliable performance gains for all evaluated backbones on both datasets. In particular, many baseline MLLMs exhibit relatively low recall, which can be attributed to their tendency to under-

detect anomalies when visual evidence is weak or ambiguous. By introducing DBT mechanism to control the injection of visual prompts, EAGLE improves recall in a stable manner, thereby enhancing overall anomaly detection performance.

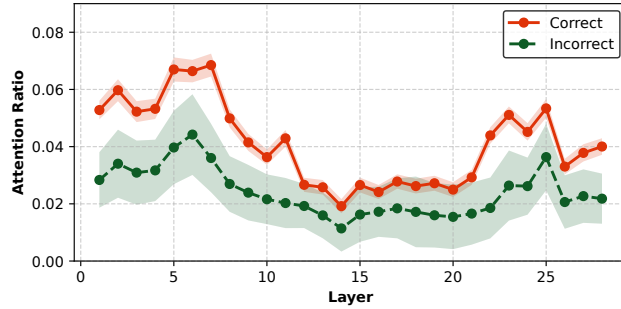
Notably, EAGLE operates in a tuning-free manner and does not require any task-specific parameter updates. As shown in Tab. 2, Despite this constraint, it achieves competitive performance compared to fine-tuned approaches. For example, EAGLE attains the best results on VisA and shows comparable performance to OmniAD [42] on MVTec-AD. While both methods are built upon the Qwen2.5-VL-7B [2] backbone, OmniAD relies on task-specific fine-tuning and GRPO-based optimization, whereas EAGLE improves anomaly detection performance using a frozen MLLMs.

## 4.3. Ablation Studies.

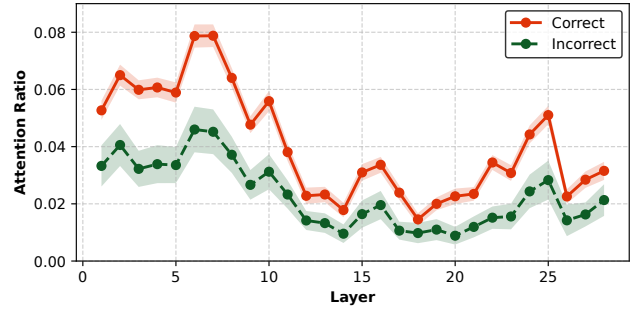
We validate the effectiveness of each step in the EAGLE on Qwen2.5-VL-7B[2] through ablation studies.

**Impact of Expert model.** Tab. 3 compares model performance under different prompting modalities. Visual-only prompting provides certain performance gains but leads to reduced accuracy on VisA, as the expert model generates anomaly maps for all images, including normal samples, which may introduce misleading visual cues. In contrast, the complete method with DBT, which combines visual and textual prompting, achieves more stable improvements. By injecting visual prompts only for images classified as anomalous, DBT effectively reduces false positives and improves overall detection performance.

**Impact of CAAS.** Tab. 4 evaluates the effect of CAAS by amplifying attention to visual tokens ( $\alpha = 0.6$ ). The results indicate that strengthening visual attention contributes to improved performance. We further examine suppressing attention to erroneous textual priors ( $\beta = -0.4$ ), as well as jointly modulating both visual and textual attention. While all these strategies outperform the baseline, visual-only amplification



(a) Qwen2.5VL-7B



(b) InternVL3-8B

Figure 8. Attention ratios to ground-truth anomalous regions across transformer layers for multiple MLLMs. Correctly answered samples consistently exhibit higher attention ratios than incorrectly answered ones. Shaded regions indicate standard deviation.

Table 3. Ablation study on the expert model under different settings, including no expert, visual-only prompts, textual-only prompts, and combined visual and textual prompts.

Setting	MVTec-AD		VisA	
	Accuracy	F1	Accuracy	F1
Baseline	85.9	88.3	76.1	69.4
Expert (Visual only)	75.3	89.7	68.3	76.5
Expert (Textual only)	82.4	99.5	65.4	77.3
<b>Expert (Visual + Textual)</b>	<b>93.1</b>	<b>96.2</b>	<b>88.3</b>	<b>85.7</b>

Table 4. Ablation study on CAAS.

Setting	MVTec-AD		VisA	
	Accuracy	F1	Accuracy	F1
Baseline	93.1	96.2	<b>88.3</b>	<b>85.7</b>
Visual + Textual	94.2	96.4	85.8	82.5
Text	93.9	96.7	87.1	84.2
<b>Visual</b>	<b>94.6</b>	<b>96.7</b>	86.7	83.6

yields the most effective improvement. We further provide an ablation study on the parameter  $a$  in the Appendix. 6.2.2.

#### 4.4. Analysis And Discussion

To investigate whether incorrect predictions are associated with improper attention behaviors, we analyze the visual attention allocated to ground-truth anomalous regions across Transformer layers, focusing on anomalous samples in the test set. Specifically, we define an *attention ratio* to quantify the degree to which the model focuses on true defect regions as  $AR^{(l)} = \frac{\sum_{p \in \mathcal{G}} A_p^{(l)}}{\sum_{p \in \mathcal{I}} A_p^{(l)}}$ , where  $A_p^{(l)}$  denotes the attention weight assigned to the  $p$ -th image token at the  $l$ -th Transformer layer when generating the final answer,  $\mathcal{G}$  represents the set of image tokens corresponding to the ground-truth anomalous region, and  $\mathcal{I}$  denotes the set of all image tokens. This ratio reflects the relative concentration of attention on the true defect region at each layer.

As shown in Fig. 8, samples that are answered correctly tend to exhibit higher attention ratios across most layers,

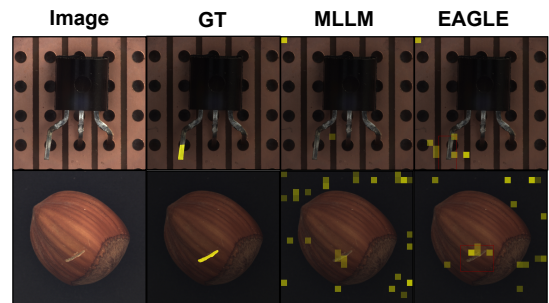


Figure 9. Qualitative analysis of EAGLE. Attention maps before and after applying EAGLE illustrate that the proposed method guides the MLLM to focus more effectively on abnormal regions.

suggesting that successful predictions are associated with a greater focus on ground-truth anomalous regions during reasoning.

To further illustrate this behavior, we visualize the attention maps  $A^{(l)}$  in Fig. 9. Compared to the original MLLM, our framework encourages more concentrated attention on defect-related regions. These results indicate that our framework can influence how visual evidence is utilized during inference, which may contribute to improved prediction outcomes.

#### 5. Conclusion

In this paper, we demonstrate that MLLMs can achieve strong industrial anomaly detection performance without any fine-tuning. By incorporating expert-guided prompting through DBT and CAAS, EAGLE improves detection accuracy and recall across multiple MLLM backbones without any parameter learning. These results suggest that structured expert guidance can serve as a practical alternative to model fine-tuning for industrial anomaly detection. In addition, our analysis reveals a clear relationship between the distribution of visual attention in MLLMs and prediction correctness. We believe this observation opens up promising directions for future work on enhancing anomaly understanding and reasoning capabilities in MLLMs.

## References

- [1] Wenbin An, Feng Tian, Sicong Leng, Jiahao Nie, Haonan Lin, Qianying Wang, Ping Chen, Xiaoqin Zhang, and Shijian Lu. Mitigating object hallucinations in large vision-language models with assembly of global and local attention. In *Proceedings of the IEEE/CVF Conference on Computer Vision and Pattern Recognition (CVPR)*, pages 29915–29926, 2025. 2
- [2] Shuai Bai, Keqin Chen, Xuejing Liu, Jialin Wang, Wenbin Ge, Sibao Song, Kai Dang, Peng Wang, Shijie Wang, Jun Tang, et al. Qwen2. 5-vl technical report. *arXiv preprint arXiv:2502.13923*, 2025. 6, 7
- [3] Kilian Batzner, Lars Heckler, and Rebecca König. Efficientad: Accurate visual anomaly detection at millisecond-level latencies. In *Proceedings of the IEEE/CVF Winter Conference on Applications of Computer Vision*, pages 128–138, 2024. 2
- [4] Paul Bergmann, Michael Fauser, David Sattlegger, and Carsten Steger. Mvtec ad—a comprehensive real-world dataset for unsupervised anomaly detection. In *Proceedings of the IEEE/CVF conference on computer vision and pattern recognition*, pages 9592–9600, 2019. 2, 6
- [5] Paul Bergmann, Michael Fauser, David Sattlegger, and Carsten Steger. Uninformed students: Student-teacher anomaly detection with discriminative latent embeddings. In *Proceedings of the IEEE/CVF conference on computer vision and pattern recognition*, pages 4183–4192, 2020. 2
- [6] Yuhao Chao, Jie Liu, Jie Tang, and Gangshan Wu. Anomaly1: A grpo-based end-to-end mllm for industrial anomaly detection. *arXiv preprint arXiv:2504.11914*, 2025. 2
- [7] Shiqi Chen, Tongyao Zhu, Ruochen Zhou, Jinghan Zhang, Siyang Gao, Juan Carlos Niebles, Mor Geva, Junxian He, Jiajun Wu, and Manling Li. Why is spatial reasoning hard for vlms? an attention mechanism perspective on focus areas. *arXiv preprint arXiv:2503.01773*, 2025. 2, 5, 6
- [8] Zhiling Chen, Hanning Chen, Mohsen Imani, and Farhad Imani. Can multimodal large language models be guided to improve industrial anomaly detection? *arXiv preprint arXiv:2501.15795*, 2025. 2, 7
- [9] Ronald Aylmer Fisher and Leonard Henry Caleb Tippett. Limiting forms of the frequency distribution of the largest or smallest member of a sample. In *Mathematical proceedings of the Cambridge philosophical society*, pages 180–190. Cambridge University Press, 1928. 11
- [10] Boris Gnedenko. Sur la distribution limite du terme maximum d’une serie aleatoire. *Annals of mathematics*, 44(3):423–453, 1943. 11
- [11] Yash Goyal, Tejas Khot, Douglas Summers-Stay, Dhruv Batra, and Devi Parikh. Making the v in vqa matter: Elevating the role of image understanding in visual question answering. In *Proceedings of the IEEE conference on computer vision and pattern recognition*, pages 6904–6913, 2017. 2
- [12] Zhaopeng Gu, Bingke Zhu, Guibo Zhu, Yingying Chen, Ming Tang, and Jinqiao Wang. Anomalygpt: Detecting industrial anomalies using large vision-language models. In *Proceedings of the AAAI conference on artificial intelligence*, pages 1932–1940, 2024. 1, 2, 7
- [13] Wei Guan, Jun Lan, Jian Cao, Hao Tan, Huijia Zhu, and Weiqiang Wang. Emit: Enhancing mllms for industrial anomaly detection via difficulty-aware grpo. *arXiv preprint arXiv:2507.21619*, 2025. 1
- [14] Shengding Hu, Yuge Tu, Xu Han, Chaoqun He, Ganqu Cui, Xiang Long, Zhi Zheng, Yewei Fang, Yuxiang Huang, Weilin Zhao, et al. Minicpm: Unveiling the potential of small language models with scalable training strategies. *arXiv preprint arXiv:2404.06395*, 2024. 6
- [15] Drew A Hudson and Christopher D Manning. Gqa: A new dataset for real-world visual reasoning and compositional question answering. In *Proceedings of the IEEE/CVF conference on computer vision and pattern recognition*, pages 6700–6709, 2019. 2
- [16] Jongheon Jeong, Yang Zou, Taewan Kim, Dongqing Zhang, Avinash Ravichandran, and Onkar Dabeer. Winclip: Zero/few-shot anomaly classification and segmentation. In *Proceedings of the IEEE/CVF Conference on Computer Vision and Pattern Recognition*, pages 19606–19616, 2023. 2
- [17] Xi Jiang, Ying Chen, Qiang Nie, Jianlin Liu, Yong Liu, Chengjie Wang, and Feng Zheng. Toward multi-class anomaly detection: Exploring class-aware unified model against inter-class interference. *arXiv preprint arXiv:2403.14213*, 2024. 2
- [18] Xi Jiang, Jian Li, Hanqiu Deng, Yong Liu, Bin-Bin Gao, Yifeng Zhou, Jialin Li, Chengjie Wang, and Feng Zheng. Mmad: The first-ever comprehensive benchmark for multimodal large language models in industrial anomaly detection. *arXiv e-prints*, pages arXiv–2410, 2024. 1, 2, 6
- [19] Yuqi Jiang, Xudong Lu, Qian Jin, Qi Sun, Hanming Wu, and Cheng Zhuo. Fabgpt: An efficient large multimodal model for complex wafer defect knowledge queries. In *Proceedings of the 43rd IEEE/ACM International Conference on Computer-Aided Design*, pages 1–8, 2024. 2
- [20] Er Jin, Qihui Feng, Yongli Mou, Gerhard Lakemeyer, Stefan Decker, Oliver Simons, and Johannes Stegmaier. Logicad: Explainable anomaly detection via vlm-based text feature extraction. In *Proceedings of the AAAI Conference on Artificial Intelligence*, pages 4129–4137, 2025. 2
- [21] Sicong Leng, Hang Zhang, Guanzheng Chen, Xin Li, Shijian Lu, Chunyan Miao, and Lidong Bing. Mitigating object hallucinations in large vision-language models through visual contrastive decoding. In *Proceedings of the IEEE/CVF Conference on Computer Vision and Pattern Recognition*, pages 13872–13882, 2024. 5
- [22] Xurui Li, Ziming Huang, Feng Xue, and Yu Zhou. Musc: Zero-shot industrial anomaly classification and segmentation with mutual scoring of the unlabeled images. In *The Twelfth International Conference on Learning Representations*, 2024. 2
- [23] Xiaofan Li, Zhizhong Zhang, Xin Tan, Chengwei Chen, Yanyun Qu, Yuan Xie, and Lizhuang Ma. Promptad: Learning prompts with only normal samples for few-shot anomaly detection. In *Proceedings of the IEEE/CVF Conference on Computer Vision and Pattern Recognition*, pages 16838–16848, 2024. 2
- [24] Yuanze Li, Haolin Wang, Shihao Yuan, Ming Liu, Debin Zhao, Yiwen Guo, Chen Xu, Guangming Shi, and Wang-

- meng Zuo. Myriad: Large multimodal model by applying vision experts for industrial anomaly detection. *arXiv preprint arXiv:2310.19070*, 2023. 1, 2, 7
- [25] Yanhui Li, Yunkang Cao, Chengliang Liu, Yuan Xiong, Xinghui Dong, and Chao Huang. Iad-r1: Reinforcing consistent reasoning in industrial anomaly detection. *arXiv preprint arXiv:2508.09178*, 2025. 1
- [26] Yuanze Li, Shihao Yuan, Haolin Wang, Qizhang Li, Ming Liu, Chen Xu, Guangming Shi, and Wangmeng Zuo. Triad: Empowering lmm-based anomaly detection with expert-guided region-of-interest tokenizer and manufacturing process. In *Proceedings of the IEEE/CVF International Conference on Computer Vision*, pages 21917–21926, 2025. 1
- [27] Tsung-Yi Lin, Michael Maire, Serge Belongie, James Hays, Pietro Perona, Deva Ramanan, Piotr Dollár, and C Lawrence Zitnick. Microsoft coco: Common objects in context. In *European conference on computer vision*, pages 740–755. Springer, 2014. 2
- [28] Haotian Liu, Chunyuan Li, Yuheng Li, and Yong Jae Lee. Improved baselines with visual instruction tuning. In *Proceedings of the IEEE/CVF conference on computer vision and pattern recognition*, pages 26296–26306, 2024. 6
- [29] Haotian Liu, Chunyuan Li, Yuheng Li, Bo Li, Yuanhan Zhang, Sheng Shen, and Yong Jae Lee. Llanext: Improved reasoning, ocr, and world knowledge, 2024. 6
- [30] Sassan Mokhtar, Arian Mousakhan, Silvio Galesso, Jawad Tayyub, and Thomas Brox. Detect, classify, act: Categorizing industrial anomalies with multi-modal large language models. In *Proceedings of the Computer Vision and Pattern Recognition Conference*, pages 4058–4067, 2025. 2
- [31] Karsten Roth, Latha Pemula, Joaquin Zepeda, Bernhard Schölkopf, Thomas Brox, and Peter Gehler. Towards total recall in industrial anomaly detection. In *Proceedings of the IEEE/CVF conference on computer vision and pattern recognition*, pages 14318–14328, 2022. 2, 3, 6
- [32] Amanpreet Singh, Vivek Natarajan, Meet Shah, Yu Jiang, Xinlei Chen, Dhruv Batra, Devi Parikh, and Marcus Rohrbach. Towards vqa models that can read. In *Proceedings of the IEEE/CVF conference on computer vision and pattern recognition*, pages 8317–8326, 2019. 2
- [33] Chenxi Wang, Xiang Chen, Ningyu Zhang, Bozhong Tian, Haoming Xu, Shumin Deng, and Huajun Chen. Mllm can see? dynamic correction decoding for hallucination mitigation. *arXiv preprint arXiv:2410.11779*, 2024. 5
- [34] Sangmin Woo, Donguk Kim, Jaehyuk Jang, Yubin Choi, and Changick Kim. Don’t miss the forest for the trees: Attentional vision calibration for large vision language models. In *Findings of the Association for Computational Linguistics: ACL 2025*, pages 1927–1951, 2025. 2
- [35] Jiacong Xu, Shao-Yuan Lo, Bardia Safaei, Vishal M Patel, and Isht Dwivedi. Towards zero-shot anomaly detection and reasoning with multimodal large language models. In *Proceedings of the Computer Vision and Pattern Recognition Conference*, pages 20370–20382, 2025. 1, 2
- [36] Hao Yin, Guangzong Si, and Zilei Wang. ClearSight: Visual signal enhancement for object hallucination mitigation in multimodal large language models. In *Proceedings of the Computer Vision and Pattern Recognition Conference*, pages 14625–14634, 2025. 5
- [37] Peter Young, Alice Lai, Micah Hodosh, and Julia Hockenmaier. From image descriptions to visual denotations: New similarity metrics for semantic inference over event descriptions. *Transactions of the association for computational linguistics*, 2:67–78, 2014. 2
- [38] Vitjan Zavrtanik, Matej Kristan, and Danijel Skočaj. Draem-a discriminatively trained reconstruction embedding for surface anomaly detection. In *Proceedings of the IEEE/CVF international conference on computer vision*, pages 8330–8339, 2021. 2
- [39] Peijian Zeng, Feiyan Pang, Zhanbo Wang, and Aimin Yang. Lr-iad: Mask-free industrial anomaly detection with logical reasoning. *arXiv preprint arXiv:2504.19524*, 2025. 2, 7
- [40] Yiheng Zhang, Yunkang Cao, Xiaohao Xu, and Weiming Shen. Logiccode: an llm-driven framework for logical anomaly detection. *IEEE Transactions on Automation Science and Engineering*, 2024. 2
- [41] Zongyun Zhang, Jiacheng Ruan, Xian Gao, Ting Liu, and Yuzhuo Fu. Eiad: Explainable industrial anomaly detection via multi-modal large language models. *arXiv preprint arXiv:2503.14162*, 2025. 1, 2
- [42] Shifang Zhao, Yiheng Lin, Lu Han, Yao Zhao, and Yunchao Wei. Omniad: Detect and understand industrial anomaly via multimodal reasoning. *arXiv preprint arXiv:2505.22039*, 2025. 1, 2, 7
- [43] Qihang Zhou, Guansong Pang, Yu Tian, Shibo He, and Jiming Chen. Anomalyclip: Object-agnostic prompt learning for zero-shot anomaly detection. *arXiv preprint arXiv:2310.18961*, 2023. 2
- [44] Jinguo Zhu, Weiyun Wang, Zhe Chen, Zhaoyang Liu, Shenglong Ye, Lixin Gu, Hao Tian, Yuchen Duan, Weijie Su, Jie Shao, et al. Internvl3: Exploring advanced training and test-time recipes for open-source multimodal models. *arXiv preprint arXiv:2504.10479*, 2025. 6
- [45] Yang Zou, Jongheon Jeong, Latha Pemula, Dongqing Zhang, and Onkar Dabeer. Spot-the-difference self-supervised pre-training for anomaly detection and segmentation. In *European conference on computer vision*, pages 392–408. Springer, 2022. 2, 6

## 6. Appendix

### 6.1. Limitations

**Sensitivity to Distribution Shift.** DBT mechanism relies on training set normal samples for threshold estimation. When test samples exhibit significant distribution shift, the estimated threshold may become unreliable, generating erroneous linguistic priors that exacerbate MLLMs hallucinations rather than mitigate them. Future work should explore adaptive thresholding strategies to handle distribution shifts.

**MLLMs Dependency.** EAGLE’s performance is inherently limited by the capabilities of the underlying MLLMs backbone. Issues such as inadequate visual grounding, limited reasoning capacity, or inherent biases in the pretrained model directly affect our framework’s effectiveness. As MLLMs architectures continue to evolve, EAGLE’s performance may improve correspondingly.

### 6.2. Additional Analysis

#### 6.2.1. Further Analyses and Discussions on Distribution-Based Thresholdin mechanism

**Extreme Value Distributions.** The goal of extreme value theory (EVT) is to model the statistical behavior of extreme events. A classical result established by Fisher and Tippett [9] and later formalized by Gnedenko [10] states that if  $X_1, \dots, X_n$  are independent and identically distributed (i.i.d.) random variables with a common distribution function  $F$ , and

$$X_{(n)} = \max(X_1, \dots, X_n), \quad (10)$$

denotes their maximum, then under mild regularity conditions, the properly normalized maximum converges in distribution to a non-degenerate limit law  $G(x)$ . This limiting law is called an **Extreme Value Distribution (EVD)**, which takes the following general form:

$$G_\gamma(x) = \exp \left[ -(1 + \gamma x)^{-\frac{1}{\gamma}} \right], \quad \gamma \in \mathbb{R}, \quad 1 + \gamma x > 0, \quad (11)$$

where  $\gamma$  is known as the *extreme value index*, determining the shape of the tail behavior. All extreme values of common standard distributions follow one of these forms of  $G_\gamma(x)$ , depending on their original distribution  $F(x)$ .

In the context of industrial anomaly detection, the applicability of EVT is further supported by the characteristics of commonly used inspection datasets. In many industrial settings, image acquisition is conducted under strictly controlled conditions, such as fixed illumination, viewpoint, and background. As a result, normal samples within the same category tend to exhibit limited intra-class variation and can be reasonably approximated as being drawn from a common underlying distribution.

Under this assumption, the image-level anomaly score of a normal sample, which is defined as the maximum over

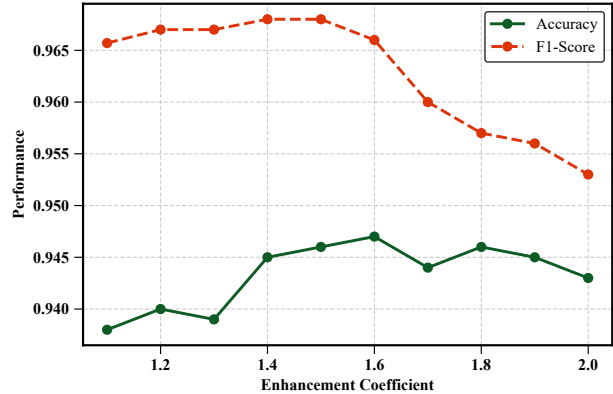


Figure 10. Ablation study of scaling factor  $\alpha$  on the MVTEC.

patch-level anomaly scores (Eq. 3), naturally corresponds to an extreme statistic (Eq. 10). According to EVT, the distribution of such maxima can be well modeled by an extreme value distribution, regardless of the specific form of the underlying patch-level score distribution, provided mild regularity conditions are satisfied. This property makes EVT particularly suitable for modeling the tail behavior of anomaly scores derived from normal training data.

In our setting, the anomaly scores computed from unsampled patches of normal training images form a large collection of extreme observations. Fitting an extreme value distribution to these scores allows us to capture the statistical characteristics of normal extremes and estimate a decision threshold in a principled manner. Samples whose anomaly scores deviate significantly from this distribution are therefore more likely to correspond to true defects, providing a statistically grounded basis for anomaly discrimination.

#### 6.2.2. Further Analyses and Discussions on Confidence-Aware Attention Sharpening

Furthermore, we conduct ablation studies on parameter  $\alpha$  to investigate its impact on model performance. As shown in Figure 10, increasing  $\alpha$  within a moderate range ( $0 < \alpha < 1$ ) leads to continuous performance improvement, demonstrating that moderately enhancing visual attention can effectively mitigate hallucinations caused by erroneous linguistic priors.

However, when  $\alpha$  exceeds 0.5, performance begins to decline. This trend is likely caused by excessive amplification of visual features disrupting the balance between visual and linguistic information. These observations further support our core design principle that visual and linguistic modalities should be dynamically balanced rather than excessively biased toward a single modality. Moderate visual enhancement enables the model to correct unreliable linguistic priors, while excessive intervention disrupts the original multimodal reasoning structure.

---

**Algorithm 1** Expert model pseudo-code.

---

**Input:** Pretrained  $\phi$ , hierarchies  $\mathcal{J}$ , nominal data  $\mathcal{X}_N$ , stride  $s$ , patchsize  $p$ , coreset target  $l$ , random linear projection  $\psi$ .

**Output:** Patch-level Memory bank  $\mathcal{M}$ , image-level anomaly scores.

/\*Step 1: Extract patches and record indices/

$\mathcal{M} \leftarrow \{\}$

$\mathcal{I} \leftarrow \{\}$

$\mathcal{R} \leftarrow \{\}$

▷ Image-patch index mapping  
▷ Reverse mapping: patch  $\rightarrow$  (image, patch\_idx)

**for**  $i = 0, \dots, |\mathcal{X}_N| - 1$  **do**

$x_i \leftarrow \mathcal{X}_N[i]$

$\mathcal{P}_i \leftarrow \mathcal{P}_{s,p}(\phi_{\mathcal{J}}(x_i))$

▷ Extract patches

$\mathcal{I}[i] \leftarrow \{\}$

▷ Initialize patch indices for image  $i$

**for**  $j = 0, \dots, |\mathcal{P}_i| - 1$  **do**

$m_{id} \leftarrow |\mathcal{M}|$

▷ Unique patch ID

$\mathcal{M} \leftarrow \mathcal{M} \cup \{m_{id} : \mathcal{P}_i[j]\}$

$\mathcal{I}[i] \leftarrow \mathcal{I}[i] \cup \{j : m_{id}\}$

▷ Map patch index to feature ID

$\mathcal{R}[m_{id}] \leftarrow (i, j)$

▷ Record source image and patch index

**end for**

**end for**

/\*Step 2: Apply greedy coreset selection with tracking/

$\mathcal{M}_C \leftarrow \{\}$

▷ Coreset memory bank

$\mathcal{S} \leftarrow \{\}$

▷ Sampled patches: {image\_idx: [patch\_indices]}

**for**  $k = 0, \dots, |\mathcal{X}_N| - 1$  **do**

$\mathcal{S}[k] \leftarrow []$

▷ Initialize sampled patch list for image  $k$

**end for**

**for**  $i \in [0, \dots, l - 1]$  **do**

$m_i \leftarrow \arg \max_{m \in \mathcal{M} - \mathcal{M}_C} \min_{n \in \mathcal{M}_C} \|\psi(m) - \psi(n)\|_2$

$\mathcal{M}_C \leftarrow \mathcal{M}_C \cup \{m_i\}$

▷ Track which image and patch was sampled

$(img\_idx, patch\_idx) \leftarrow \mathcal{R}[m_i]$

$\mathcal{S}[img\_idx] \leftarrow \mathcal{S}[img\_idx] \cup \{patch\_idx\}$

**end for**

$\mathcal{M} \leftarrow \mathcal{M}_C$

/\*Step 3: Compute remaining patches for each image/

$\mathcal{F}_{remain} \leftarrow \{\}$

▷ Remaining features per image

**for**  $i = 0, \dots, |\mathcal{X}_N| - 1$  **do**

$\mathcal{F}_{remain}[i] \leftarrow \{\}$

**for**  $j \in \mathcal{I}[i]$  **do**

**if**  $j \notin \mathcal{S}[i]$  **then**

$m_{id} \leftarrow \mathcal{I}[i][j]$

$\mathcal{F}_{remain}[i] \leftarrow \mathcal{F}_{remain}[i] \cup \{\mathcal{M}_{full}[m_{id}]\}$

**end if**

**end for**

**end for**

**Step 4: Compute image-level anomaly scores**

**for**  $i = 0, \dots, |\mathcal{X}_N| - 1$  **do**

$\mathcal{A}_i \leftarrow \{\}$

▷ Anomaly scores for all patches in image  $i$

**for**  $f \in \mathcal{F}_{remain}[i]$  **do**

$m^* \leftarrow \arg \min_{m \in \mathcal{M}} \|f - m\|_2$

▷ Nearest neighbor in memory

$s_f \leftarrow \|f - m^*\|_2$

▷ Patch-level anomaly score

$\mathcal{A}_i \leftarrow \mathcal{A}_i \cup \{(f, s_f)\}$

**end for**

$(f_i^*, m_i^*) \leftarrow \arg \max_{f \in \mathcal{A}_i} \arg \min_{m \in \mathcal{M}} \|f - m\|_2$

▷ Image-level score

$s_i \leftarrow \|f_i^* - m_i^*\|_2$

**end for**

**return**  $\mathcal{M}, \{s_i\}_{i=0}^{|\mathcal{X}_N|-1}$

---

## 6.3. Prompt detail

### 6.3.1. Prompt Design Details

All experiments in this paper follow a unified prompting scheme to ensure fair and consistent evaluation across different MLLM backbones. The prompt is constructed by combining a fixed instruction, optional expert-generated cues, and a question requiring a binary decision.

**System Instruction.** You are my industrial image inspection assistant. You will receive multiple images simultaneously, including a template image, a query image, and a query image with red bounding boxes. Based on the input images and the accompanying textual information, answer the given question. The question is multiple-choice. Respond only with the letter of the correct option (e.g., A, B, C, or D). Do not include explanations or extra text.

**Expert-Guided Prompts.** When available, expert model outputs are incorporated into the prompt in two forms:

- **Textual Prompt.**
  - **Normal Prompt.** The query image is predicted as anomalous. The position of the red bounding box on the query image is the predicted defect location. Answer with the option's letter from the given choices directly! Is there any defect in the object? A. Yes. B. No.
  - **Abnormal Prompt.** The query image is predicted as normal. Answer with the option's letter from the given choices directly! Is there any defect in the object? A. Yes. B. No.
- **Visual Prompts.** see Fig. 13

To avoid misleading cues, visual prompts are provided only for images classified as anomalous by the expert model.

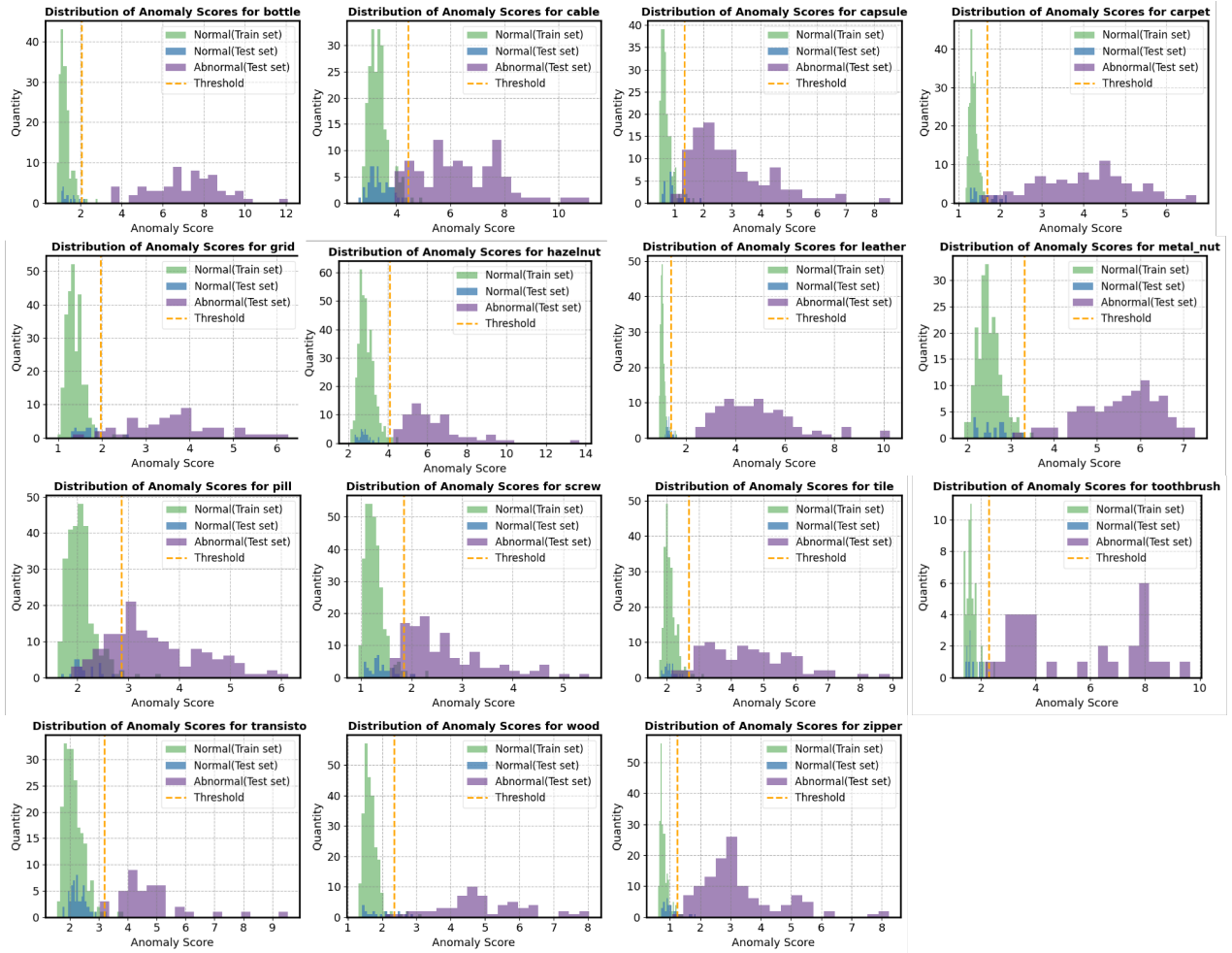


Figure 11. Anomaly score distribution of MVTec-AD.

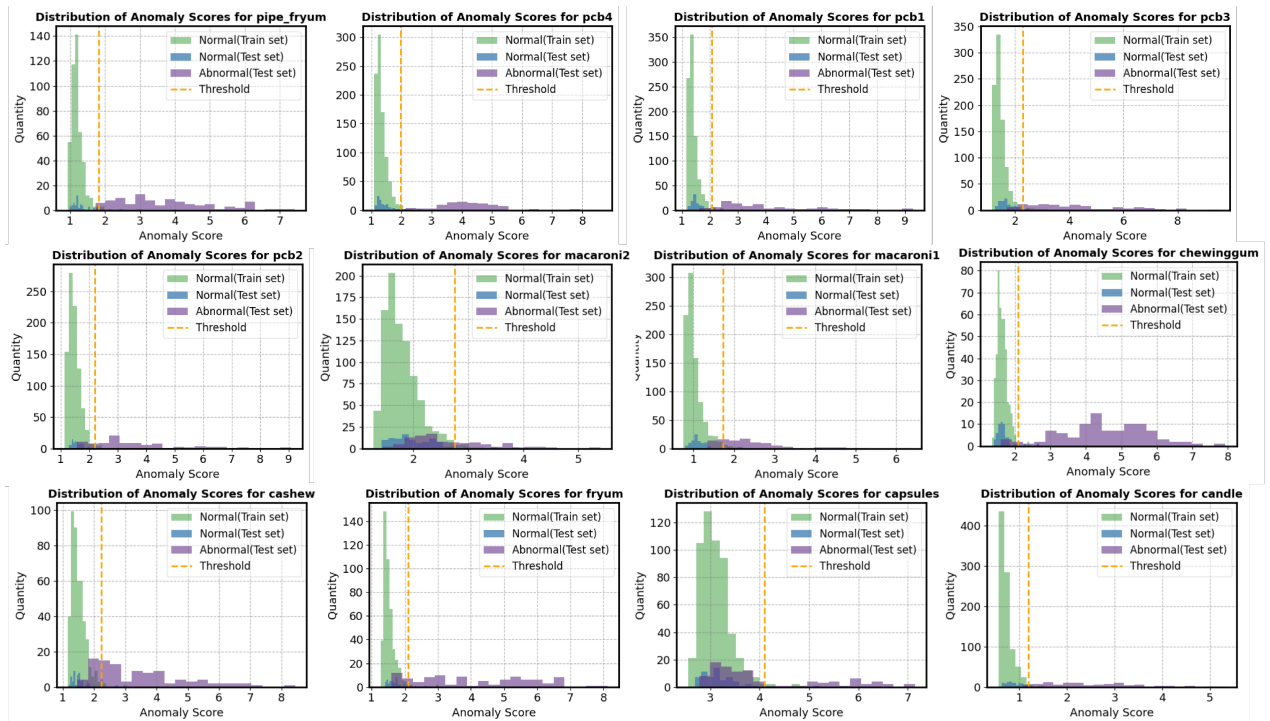


Figure 12. Anomaly score distribution of VisA

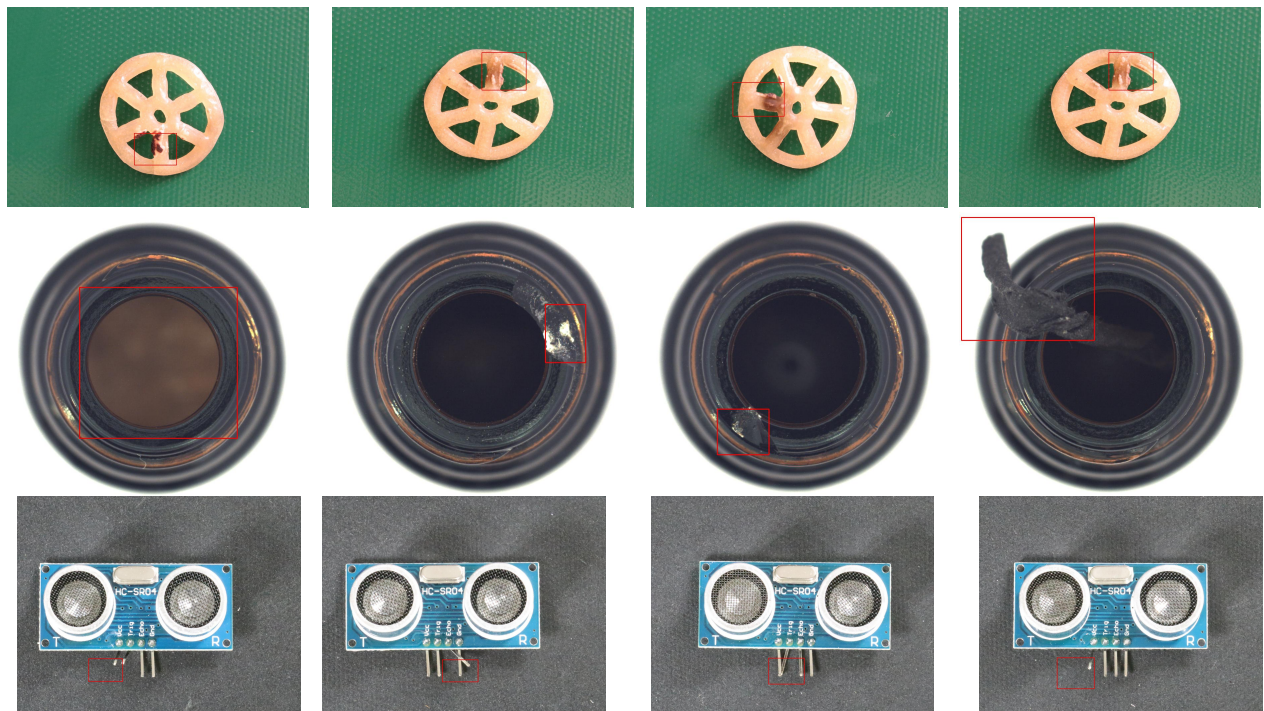


Figure 13. Visual prompt